

Neutron Diffraction Residual Strain Measurements of Molybdenum Carbide-Based Solid Oxide Fuel Cell Anode Layers with Metal Oxides on Hastelloy X

N.H. Faisal¹ · R. Ahmed² · A.K. Prathuru¹ · S.P. Katikaneni³ · M.F.A. Goosen⁴ · S.Y. Zhang⁵

Received: 10 June 2016 / Accepted: 15 May 2017 / Published online: 31 May 2017
© The Author(s) 2017. This article is an open access publication

Abstract Thermal spray deposition processes impart residual stress in layered Solid Oxide Fuel Cells (SOFC) materials and hence influence the durability and efficiency of the cell. The current study which is the first of its kind in published literature, reports results on using a neutron diffraction technique, to non-destructively evaluate the through thickness strain measurement in plasma sprayed (as-sprayed) anode layer coatings on a Hastelloy®X substrate. Through thickness neutron diffraction residual strain measurements were done on three different anode coatings (Mo-Mo₂C/Al₂O₃, Mo-Mo₂C/ZrO₂ and Mo-Mo₂C/TiO₂) using the vertical scan mode. The three anode coatings (developed through optimised process parameters) investigated had porosities as high as 20%, with thicknesses between 200 µm to 300 µm deposited on 4.76 mm thick Hastelloy®X substrate discs of 20 mm diameter. The results showed that while the through thickness residual strain in all three anodes was dissimilar for the investigated crystallographic planes, on average it was tensile. Other measurements include X-ray diffraction, nanoindentation and SEM microscopy. As the anode layer microstructures

are complex (includes bi-layer alternate phases), non-destructive characterisation of residual strain, e.g. using neutron diffraction, provides a useful measure of through thickness strain profile without altering the stress field in the SOFC electrode assembly.

Keywords SOFC · Neutron scattering · Residual strain · Plasma spray · Nanoindentation

Introduction

The development of anode materials with high durability and lower operating temperatures is a key technical challenge facing solid oxide fuel cell (SOFC) technology [1]. Low mechanical strength and anode deterioration represent some of these inherent challenges. The high operating temperatures (e.g. 800 °C to 1000 °C) place additional durability requirements on SOFCs materials [1]. The change of residual stresses in SOFC electrode materials while in operation at high temperature is related to the changes in the Young's modulus, thermal expansion mismatch, micro-defects and possible creeping of porous substrate [2]. Reducing the operating temperature to intermediate range can lower the cost but also reduce the reaction rate [1]. Recent articles [3] summarised most of the known SOFC materials (anode, electrolytes, cathodes, interconnects) and their manufacturing alternatives, relevant to modern requirements.

It is important to note that techniques such as tape casting, screen printing, and co-sintering of layers are the state-of-the-art processing methods for the production of SOFC single cells, and therefore widely adopted and intensively investigated [3]. However, these techniques face some problems e.g. increased capital cost due to high temperature firing, thermal expansion mismatch strain and cracking during high-

✉ N.H. Faisal
N.H.Faisal@rgu.ac.uk

¹ School of Engineering, Robert Gordon University, Garthdee Road, Aberdeen AB10 7GJ, UK

² School of Engineering and Physical Sciences, Heriot-Watt University, Edinburgh EH14 4AS, UK

³ Research & Development Centre, Saudi Aramco, Dhahran 31311, Saudi Arabia

⁴ Office of Research & Graduate Studies, Alfaisal University, P.O. Box 50927, Riyadh 11533, Saudi Arabia

⁵ ISIS Neutron Source, Science and Technology Facilities Council (STFC), Rutherford Appleton Laboratory, Didcot OX11 0QX, UK

temperature firing steps, inter-reaction between adjacent cell layers at high-temperature firing steps, and limitation of high-temperature sintering of anode and metallic interconnect materials. But in recent times, alternative methods are in use e.g. thermal spray technique [2] has been considered to manufacture electrode layers in SOFCs. One of the key factors influencing the durability of thermally sprayed SOFCs is the through thickness residual stress profile in the coating substrate system. It is also known that the residual stress values of SOFC electrodes (or any other materials) are very much dependent upon the measurement method (e.g. X-ray diffraction [2, 4–17], synchrotron X-ray radiation [18–21], curvature method [15, 22–26], finite element [27, 28], numerical [16, 29], focused ion beam milling and digital image correlation [30], white light interferometry [25], nanoindentation [25, 28], and neutron diffraction [31] methods). Furthermore, thermal spray deposition processes due to high cooling rates of the impacting particles (lamella) impart residual stress in the layered SOFC materials and hence influence the durability and efficiency of the cell. The residual stresses in plasma sprayed coatings can be sub-divided into two main contributions: quenching stress or primary stress at the lamella level, and thermal mismatch stress or secondary stress.

There are a few literature reports where residual stresses have been investigated using only X-ray diffraction (XRD) technique in the layered SOFC materials deposited through thermal spray method [2, 4, 5]. It has been argued that X-ray (synchrotron) techniques results in radiation that does not penetrate very well into the SOFC electrode subsurface layers including the bottom porous substrate support [2, 4, 5]. However, more recently *in-situ* neutron diffraction technique [31] was used to do visualization of the phase evolutions in SOFC materials at high temperatures, along with the analysis of the diffusion activities of transition metal ions that reveal the reaction mechanism and kinetics in the composite cathode for SOFC. Likewise, neutron diffraction has been argued to be superior for characterisation purposes as the high flux and deep penetration of neutrons facilitate the study of bulk materials at elevated temperatures, enabling it to derive the structural evolution during heating, annealing and cooling [31]. Although neutron diffraction has been used to investigate strain in the past in thermally sprayed coating-substrate systems [32–34], through thickness evaluation of strains in the thermally sprayed SOFC anode/interconnect system has not yet been realized.

Molybdenum-carbide based layers can be employed in anodes for hydrocarbon oxidation, as it shows good tolerance towards sulfidation and carbon deposition. It has been demonstrated that at elevated pressure, the choice of the support for the Mo_2C dry reforming catalyst is crucial to catalyst stability. The order of catalyst stability was found to be $\text{Mo}_2\text{C}-\text{Al}_2\text{O}_3 > \text{Mo}_2\text{C}-\text{ZrO}_2 > \text{Mo}_2\text{C}-\text{TiO}_2$, with the first being the most stable. Considering such key factors, these composite

materials can potentially be used for an improved anode performance in SOFCs [35] as previously indicated by the authors. It is important to note that in anode layer, the deposited splats play a crucial role in determining the physical properties of the coatings. Furthermore, molybdenum-carbide based anode materials with various metal oxide precursors offer major advantages of higher mechanical strength and improved thermal and wear resistance properties in comparison to other materials. Therefore, the scope of such work includes the need to characterise the residual strain in molybdenum carbide-based SOFC anode layers with various metal oxides on Hastelloy substrate (normally used as interconnect in SOFCs).

The aim of the current study, which is the first detailed investigation of its kind in published literature, was to non-destructively investigate, using neutron diffraction, the relative changes in the through thickness residual strain and stress profile in an anode (deposited using air plasma spray (APS) technique) and interconnect system. Three different anode coatings were deposited on Hastelloy®X substrate and then strain measurements were conducted in the as-sprayed conditions, including detailed analysis of structure-property relationship.

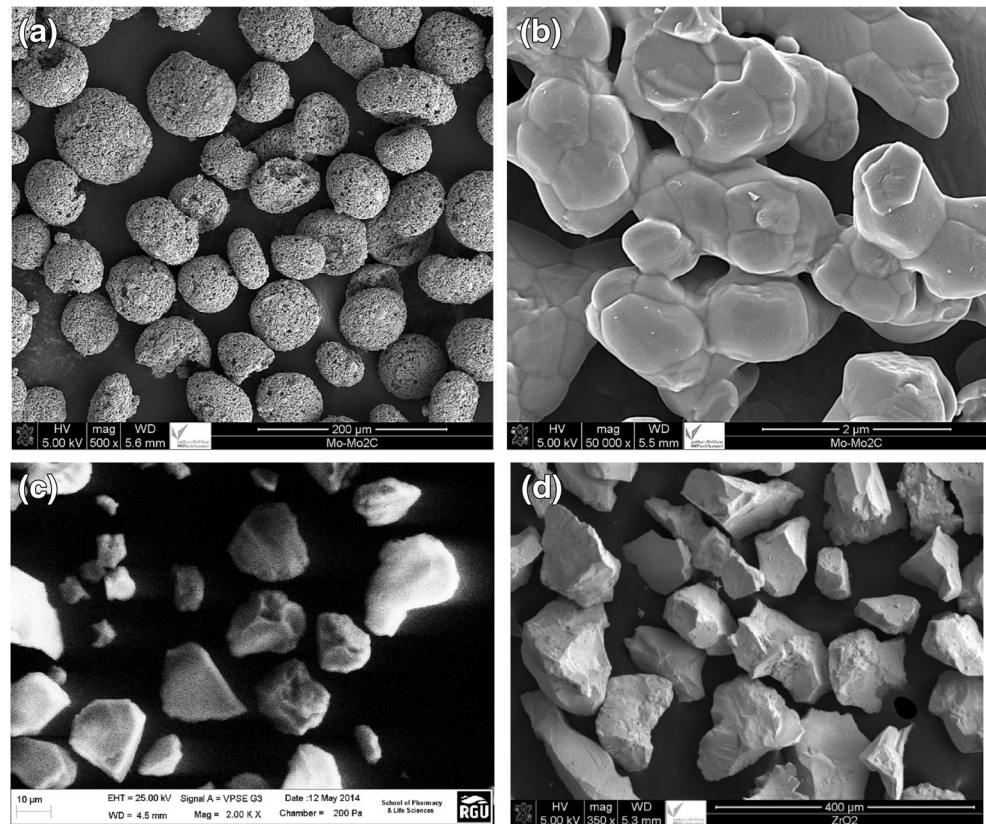
Methodology

Materials

Three composite feedstock powders ($\text{Mo}-\text{Mo}_2\text{C}/\text{Al}_2\text{O}_3$, $\text{Mo}-\text{Mo}_2\text{C}/\text{ZrO}_2$, $\text{Mo}-\text{Mo}_2\text{C}/\text{TiO}_2$) were fabricated from carbide of molybdenum powder catalyst ($\text{Mo}-\text{Mo}_2\text{C}$) and three metal oxides (e.g. Al_2O_3 , ZrO_2 , TiO_2 , each favourable for catalyst stability). The powders were subsequently employed to fabricate three diverse anodes [36]. Each of the adjusted composition anode feedstock powders was comprised of 80% $\text{Mo}-\text{Mo}_2\text{C}$ and 20% metal oxides (i.e. Al_2O_3 , ZrO_2 , TiO_2). It is noteworthy that a lower bound weight metal oxide was selected for this study to enable it to act as a catalyst with the molybdenum carbide powder. Nonetheless, research on the effects of varied weight composition can be part of an upcoming enquiry.

The selected substrates (Hastelloy®X, 20 mm diameter and 4.7 mm thick) were provided by Haynes International Limited, Manchester, UK. As a metallic matrix with carbide, the Mo with Mo_2C (i.e. $\text{Mo}-\text{Mo}_2\text{C}$, melting point was 2620 °C) feedstock powder material (Fig. 1(a, b)) was an agglomerated and sintered spheroidal powder designed for coating applications using atmospheric plasma spray (APS). The powder material (Metco 64, nominal particle size distribution $-90 + 38 \mu\text{m}$, provided by Sulzer Metco, Germany) had an elemental composition consisting of 97.3% Mo, 2.1% C, 0.1% O and 1% others. It is important to note that a “+” sign before the sieve mesh indicates the particles are retained

Fig. 1 SEM images of tested powders: (a) agglomerated and sintered Mo-Mo₂C powder; (b) corresponding zoomed view of a Mo-Mo₂C powder surface showing high porosity; (c) Al₂O₃ powder, and (d) ZrO₂ powder



by the sieve, whereas, a “-” sign before the sieve mesh indicates the particles pass through the sieve, and typically, 90% or more of the particles will lie within the indicated range. For example, if the particle size of Mo-Mo₂C is described as -90 + 38 mesh, then 90% or more of the material will pass through a 90-mesh sieve and be retained by a 38-mesh sieve.

The titanium oxide (TiO₂, melting point of 1843 °C) feed-stock powder material was available in a wide variety of colours and shapes ranging from dark grey to black, fused and crushed or agglomerated and sintered, and sizes with angular, blocky or spheroidal morphology, respectively. This agglomerated/sintered and spheroidal powder material (METCO-6231A) was supplied by Sulzer Metco, Germany and had elemental composition incorporating TiO₂ (balance wt.%), Al₂O₃ (<0.1 wt.%), Fe₂O₃ (<0.1 wt.%), SiO₂ (<0.1 wt.%) and others (<0.5 wt.%); the normal particle size distribution was -105 + 32 μm.

The white alumina (Al₂O₃, melting point of 2054 °C) feed-stock powder material (METCO-105SFP supplied by Sulzer Metco, Germany) was fused and crushed with resulting in a random angular morphology (Fig. 1(c)). The elemental composition of the powder material (particle size distribution -31 + 3.9 μm) consisted of Al₂O₃ (99.5 wt.%), Fe₂O₃ (0.03 wt.%), Na₂O (0.15 wt.%), SiO₂ (0.01 wt.%) and CaO (0.01 wt.%). The Zirconia (ZrO₂, melting point of 2700 °C) feedstock powder material which was available in a wide variety of shapes and sizes, Fig. 1(d) was supplied by Alfa Aesar

(40453), UK and consisted of Zirconium(IV) oxide, calcia stabilized, 99.4% (metals basis excluding Hf). The powder material elemental composition encompassed 96% ZrO₂ and 4% CaO, whereas, the normal particle size distribution was -100 + 325 μm.

The powders were sprayed on to the grit blasted Hastelloy®X substrate and no bond coating was used. Air plasma spray (APS) deposition was carried out at an industrial thermal spray facility (Monitor Coating Limited, UK), using a spray system (Table 1). Trials were directed to define the

Table 1 Thermal spray conditions and powders

Process parameter	Anode layer
Current	500 A
Voltage	60–70 V
Primary gas (Argon)	100 psi (0.68 MPa); 42.08 lpm
Secondary gas (Hydrogen)	50 psi (0.34 MPa); 34.2 lpm
Carrier gas (Argon)	100 psi (0.68 MPa); 19.4 lpm
Spray distance	100 mm
Feed rate	70 g/m
Spray angle	60°
Coating thickness	200 to 300 μm
APS gun	Metco 3 MB gun
APS nozzle	Metco 3M7A-GP (small bore)

operational range of the process parameters. The range of controllable factors were identified specifically feed rate, current, hydrogen flow, spray distance and spray angle. To determine the limits of the investigational factors, a key criterion was assumed that the anode layer must have high porosity. Additionally, the alteration in melting temperatures of the main feed-stock powder Mo-Mo₂C (2620 °C) and precursors [Al₂O₃ (2054 °C), ZrO₂ (2700 °C), TiO₂ (1843 °C)] can present a challenge for plasma spray deposition. Though, an optimised process parameter was chosen for each of the anode layers (Table 1).

Microstructural Characterisation

The surface characterisation of materials included scanning electron microscope (SEM) imaging using Karl Zeiss EVO LS10 and JEOL JSM 6010 LA, whereas, the X-ray diffraction (XRD) analysis using Empyrean diffractometer (PANalytical, NL) with Copper $\kappa\alpha$ radiation (1.54 Å) was employed to reveal the crystalline phase composition of the coatings. The geometry employed was a standard Bragg - Brentano reflectance geometry ($\omega - 2\theta$) in conjunction with a sample stage designed for solid objects. Patterns were acquired over the range ($2\theta = 10-75^\circ$) with a step size of 0.026° and a total collection time of 30 min.

The total porosity of coating surface (using a thresholding at 65% in the image processing software) was evaluated as the average of five area-normalized regions each from optical microscope and image analysis (IA) software (release 6.3, Lumenera Corporation). This measures all open, closed, connected elongated porosity and cannot distinguish the type, and are easily detected by image analysis due to the high degree of contrast between the dark pores (voids) and the more highly reflective coating material. It is important to note that the cross-sectional image analysis for porosity quantification is not ideal method as polished sample (intrusive method) could smear cross-section with impaired (not true representative) porosity.

Nanoindentation Tests for Hardness and Elasticity

Nanoindentation trials for hardness and elastic modulus (at 30 mN load, instrument chamber temperature 300 K) of the anode and substrate cross-sections were performed using a calibrated NanoTest™ system (Micromaterials Limited, UK) with a diamond Berkovich tip. The nanoindentation techniques were programmed as three sections of a trapezoidal shape; the first segment increased the capacity to a maximum value at a loading rate of 10 mN/s, followed by a 30-s holding section at the maximum load, and the third segment retrieved the indenter tip from the sample at an unloading rate of 10 mN/s.

Overall twenty-five assessments were done on each coating cross-section, which were dispersed in five lines of 5 measurement points each, at a specific space from the boundary, (i.e. coating surface). Depressions were spaced 22 μm apart, to circumvent any interaction of adjacent indentations. By the same token, the 10 measurements spread in two lines of 5 measurement points apiece were accomplished on each substrate cross section near the interface, at a specific distance from the interface. The force-displacement contours were examined by means of typical approaches with the area function for the Berkovich indenter whereas the modulus and hardness were investigated according to the Oliver and Pharr scheme [36]. The elastic modulus (E_i) and Poisson's ratio (ν_i) of the diamond indenter were taken as 1140 GPa and 0.07 at room temperature, whereas to calculate the elastic modulus (E_s) of the specimen, the Poisson ratio for the anode layer (ν_s) was assumed as 0.30 (Mo [37, 38]) and for the substrate (ν_s) was presumed to be 0.32 (Hastelloy [39]). Post-test residual impressions were mapped by means of an SEM.

Assessing Neutron Diffraction Residual Strain

Neutron diffraction strain measurements were implemented at the UK's Science and Technology Facilities Council's (STFC) laboratory, by means of the ENGIN-X strain diffractometer at ISIS facility [32–34]. These tests were completed at room temperature on three anode coatings (Mo-Mo₂C/Al₂O₃, Mo-Mo₂C/ZrO₂, Mo-Mo₂C/TiO₂) put down by air plasma spray (APS). The trials were conducted in a vertical scan mode with a slit gap of 200 μm in order to determine the through thickness residual strain profile of the anode-substrate system. To achieve a through-thickness residual strain profile with high resolution, a partially-submerged beam was used for measurements near the coating surface, as well as a beam submerged in the coating and substrate materials near the coating-substrate interface. A gauge volume of $0.2 \times 8 \times 4$ mm was employed [34]. Strain checks were executed at the geometric centre of the specimen. Specifics of the vertical scan technique are described in previous work [32–34].

It has been argued that if the incident beam is scanned vertically out of a horizontal surface, there is no change in diffraction angle and, hence, no pseudo-strains generated as the gauge volume moves out of the surface. It is important to note that the specimen positioner has three orthogonal linear motor drives (with nominal accuracy of 5 μm): X and Y (horizontal), and Z (vertical). The coated specimen was moved up or down in the Z -direction by at least 50 μm for depth profiling of strain in the coating and by at least 25 μm for depth profiling of strain in substrate materials (i.e. closer to interface). The incident beam was passed through a vertical and horizontal slit assembly to give a beam height at the slits of 0.2 mm. Partially submerging the gauge volume allowed the strain in the coated material (Mo-Mo₂C/Al₂O₃ with coating

thickness 250 μm), Mo-Mo₂C/TiO₂ with coating thickness 300 μm and Mo-Mo₂C/ZrO₂ with coating thickness: 220 μm) to be measured, whereas the substrate strain was mostly measured using a fully submerged gauge volume. Longer measurement times were therefore required as many measurements as necessary for strain measurement in the coating material and near interface in substrate (3 h per vertical depth).

The peaks selected for the strain examination within each anode material were such that there was minimal overlap with other crests. The strain was obtained from the shift in individual points for the anode and substrate materials using a single peak fitting routine [40, 41]. The strain free lattice parameter (d_{hkl}^0) for the coating material was found from originally mixed powder (i.e. Mo-Mo₂C/Al₂O₃, Mo-Mo₂C/ZrO₂ and Mo-Mo₂C/TiO₂). These powders were then put in a vanadium tube and their lattice factors determined. The strain free lattice parameter for the Hastelloy®X was assessed at the surface of the uncoated substrate disc. The direct elastic strain in the material in the measured path was calculated as (equation (1)):

$$\varepsilon_{hkl} = \frac{d_{hkl} - d_{hkl}^0}{d_{hkl}^0} \quad (1)$$

where d_{hkl} is the measured interplanar spacing and d_{hkl}^0 is the stress-free interplanar spacing for the given material. The elastic stress values were determined from the strain values by means of the appropriate elastic modulus (i.e. values at appropriate depth measured with a nanoindentation technique) ("Nanoindentation Tests For Hardness and Elasticity" section).

Results

Microstructure of the Anode Layer

The porosity was controlled by a selection of APS process parameters (Table 1) devoid of the need for adding a pore-forming material. The anode surfaces showed final splat structures presumably resulting from the impact of molten and semi or partially molten particles during APS thermal spraying. Additionally, SEM images of anode surfaces and cross-sections are presented in Fig. 2. In the image in Fig. 2(I), the occurrence of high density surface connected porosity was observed for all three specimens. The current study found that the anode layers had a volumetric porosity as high as $19 \pm 1\%$ for both Mo-Mo₂C/Al₂O₃ (coating thickness: 250 μm) and Mo-Mo₂C/TiO₂ (coating thickness: 300 μm) and around $16 \pm 1\%$ for Mo-Mo₂C/ZrO₂ (coating thickness: 220 μm).

Substantial surface coarseness was seen in all three anodes. Furthermore, anode layer cross-sections of the samples

(Fig. 2(II)) showed more detailed features which suggest the presence of relatively high porosity for Mo-Mo₂C/Al₂O₃ and Mo-Mo₂C/TiO₂. The observed structures included very distinct alternate layers ranging from light to dark grey in Mo-Mo₂C/Al₂O₃ and Mo-Mo₂C/TiO₂ anode layers and relatively less distinct layers in the case of Mo-Mo₂C/ZrO₂. Microcracks were also observed on the surface (Fig. 2(I) (a)).

X-ray Diffraction Analysis

The XRD spectrum of the anode surface showed the presence of dominant phase (Fig. 3). It is important to note that the infinite orientations criterion of powder diffraction may not be satisfied and so there may be pronounced textural effects observed in the XRD data; therefore, relative intensities of peaks may not match reference data and it is possible that some peaks of a phase are missing entirely due to their orientation. However, all major peaks have been clearly identified using the International Centre for Diffraction Data (ICDD) software Powder Diffraction File™ (PDF) number (00-004-0809 for Mo, 00-011-0680 for Mo₂C, 00-036-0863 for Mo_{0.42}C_{0.58}, 00-030-0029 for Al₂Mo₃C, 01-078-1070 for MoO₂, 00-049-1642 for ZrO₂, 01-083-2242 for TiO₂) used in this analysis. The Mo peak for all powders is clearly identified in Fig. 3, which was the main peak used for the strain measurements (Neutron Diffraction Measurements section). XRD analysis of anode layers in Fig. 3 indicates that Mo-Mo₂C undergoes some oxidation and decarburisation forming MoO₂ and Mo_{0.42}C_{0.58}, because of high temperature and oxygen environment during APS spraying process. This phenomenon is also frequently reported for other carbides e.g. WC-Co where oxidation and decarburisation occurs during thermal spraying process [42–44]. For specimen with blend of Mo-Mo₂C and Al₂O₃, there was some evidence of limited formation of intermetallic compound (Al₂Mo₃C). Formation of these compounds is possible due to high temperature in plasma stream, however as the dwell time (time powder spends in the heating zone) is very short, there is very little time for the formation of intermetallics. Formation of nanocrystals or amorphous phases can however result due to high temperatures and very high heating and cooling rates in plasma spraying, which normally lead to broadening of XRD peaks. However, these changes were minimal in the current study. The configuration was dominated by three strong reflections corresponding to metallic molybdenum. The segments identified in the Mo-Mo₂C/Al₂O₃ anode layer included Mo, Mo₂C, Mo_{0.42}C_{0.58}, Al₂Mo₃C and MoO₂ (Fig. 3(A)). The phases recognized in the Mo-Mo₂C/ZrO₂ anode layer encompassed Mo, MoO₂, Mo₂C, Mo_{0.42}C_{0.58} and ZrO₂ (Fig. 3(B)). The phases identified in the Mo-Mo₂C/TiO₂ anode layer involved Mo, MoO₂ and TiO₂ (Fig. 3(C)). Also, shown in Fig. 3(C) for the Mo-Mo₂C/TiO₂ anode layer, the main phase by a considerable margin was metallic

Fig. 2 SEM images of APS coated anode layer surfaces showing surface connected porosities and unmolten powder particle and cross-sections displaying features near the surfaces: (a) Mo-Mo₂C/Al₂O₃, (b) Mo-Mo₂C/ZrO₂ and (c) Mo-Mo₂C/TiO₂

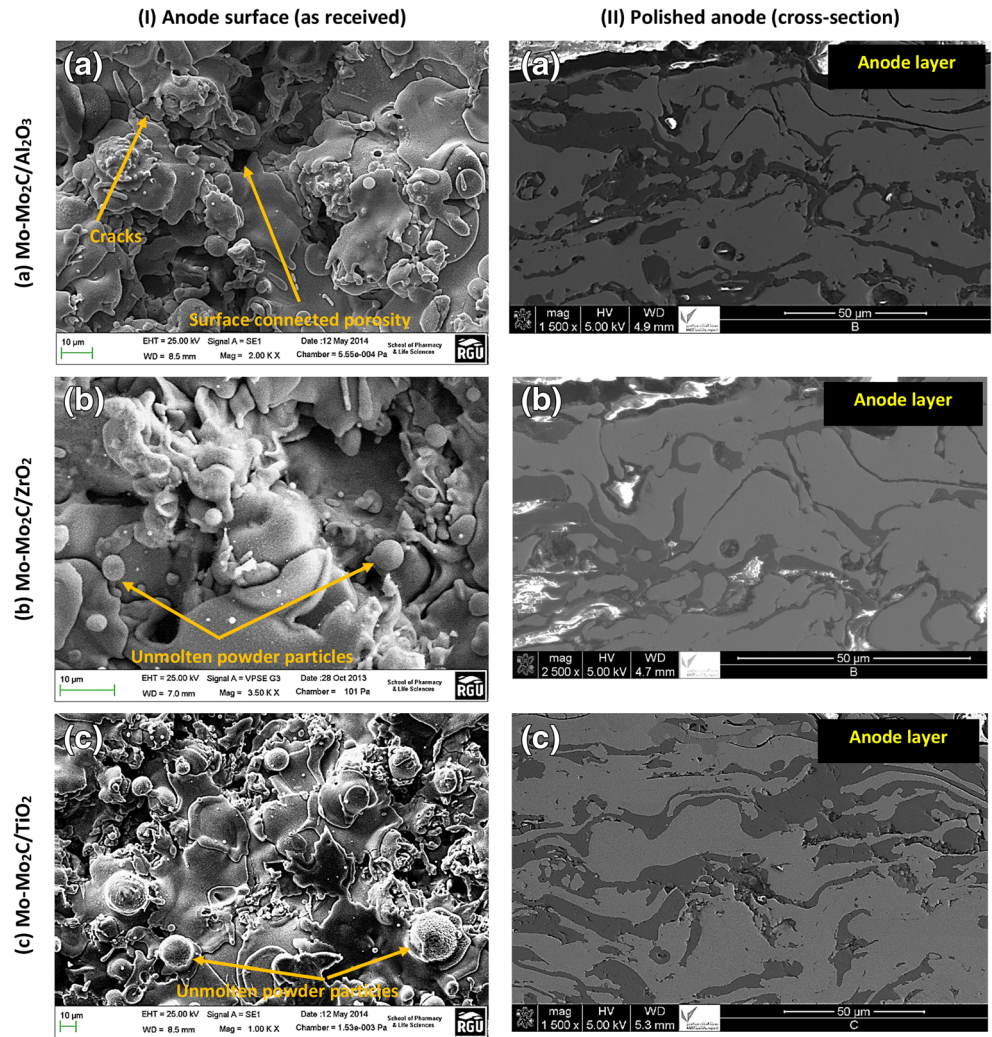
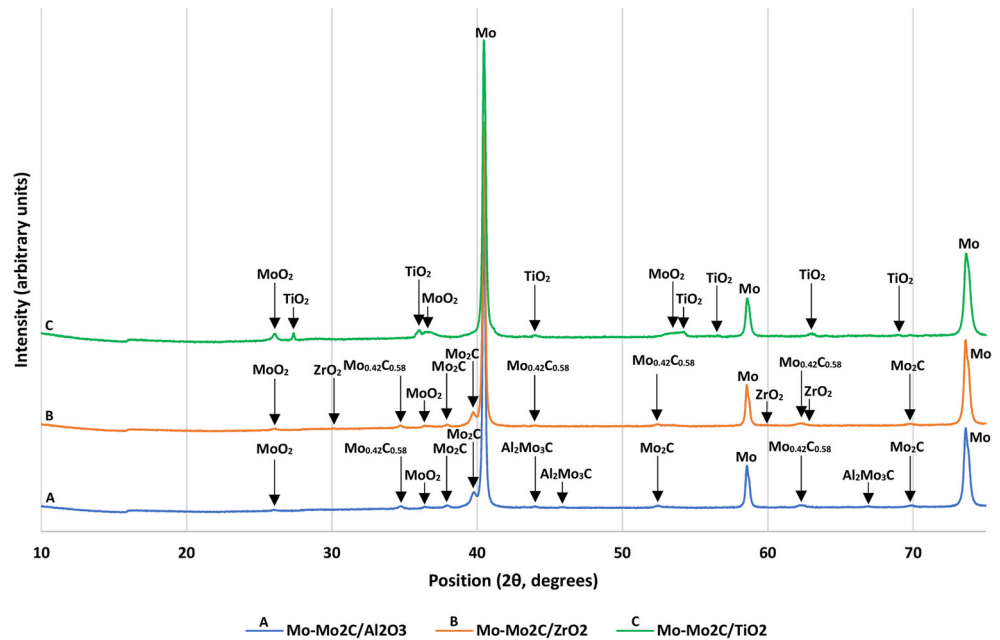


Fig. 3 X-ray diffraction of APS coated anode layers (coating surface): (A) Mo-Mo₂C/Al₂O₃, (B) Mo-Mo₂C/ZrO₂ and (C) Mo-Mo₂C/TiO₂ [three intense reflections corresponds to metallic molybdenum, Mo, in each pattern]



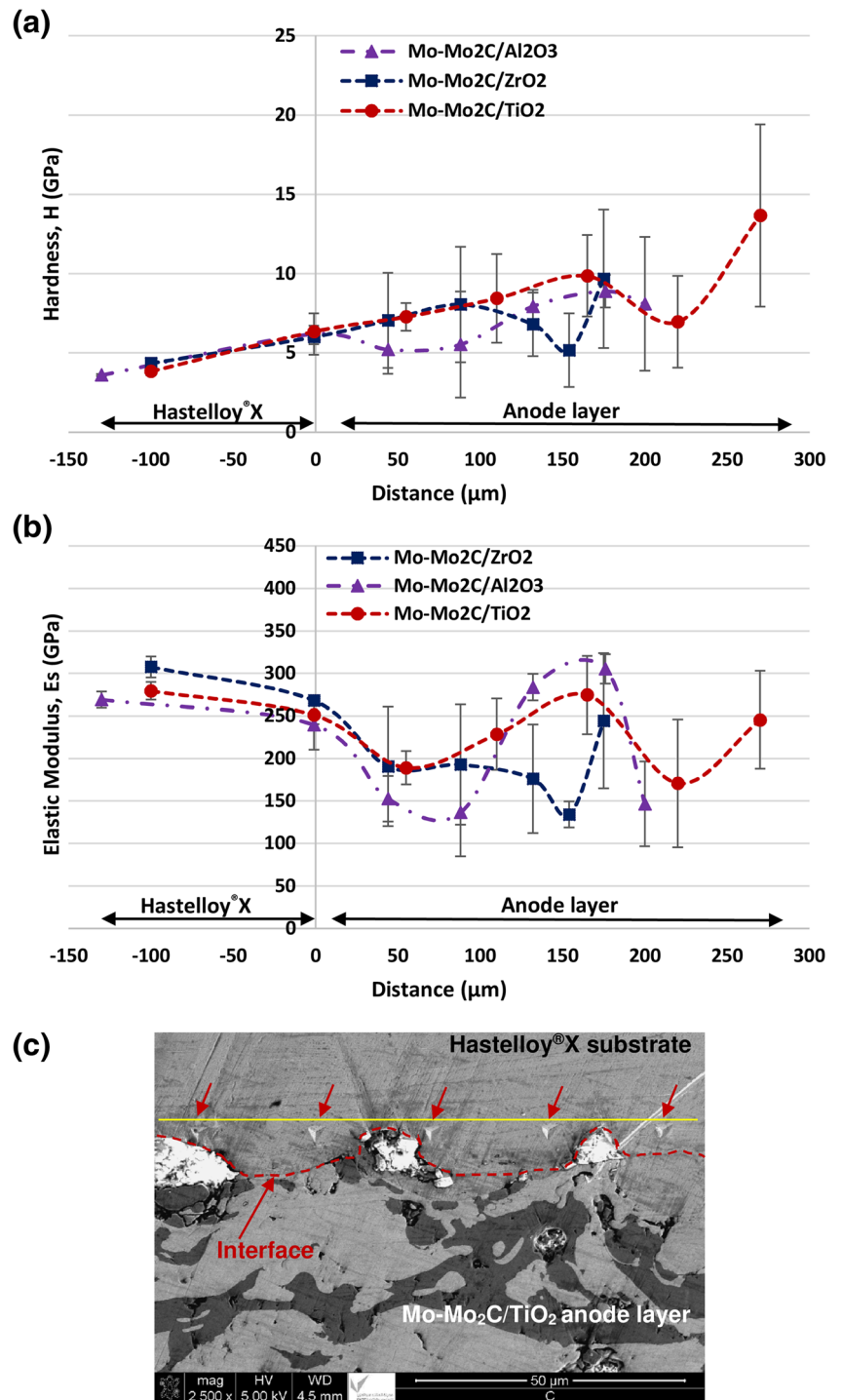
molybdenum (Mo). Unlike the previous two samples (Mo-Mo₂C/Al₂O₃ and Mo-Mo₂C/ZrO₂), there were no species of molybdenum carbide (Mo₂C) detected.

Nanoindentation Testing

The hardness results (Fig. 4(a)) principally showed that the upper layers of the coatings had higher average values than

the lower subsurface layers, with significantly high standard deviations in coating zones (e.g. Mo-Mo₂C/TiO₂) and low standard deviations in substrate zones. Each data point represented an average of 5 tests. The measurements of the elastic modulus of sample, *E_s* (Fig. 4(b)) indicated that overall the values were very similar for each coating with significantly higher standard deviations in coating zones (e.g. Mo-Mo₂C/TiO₂) and lower standard deviations in substrate zones.

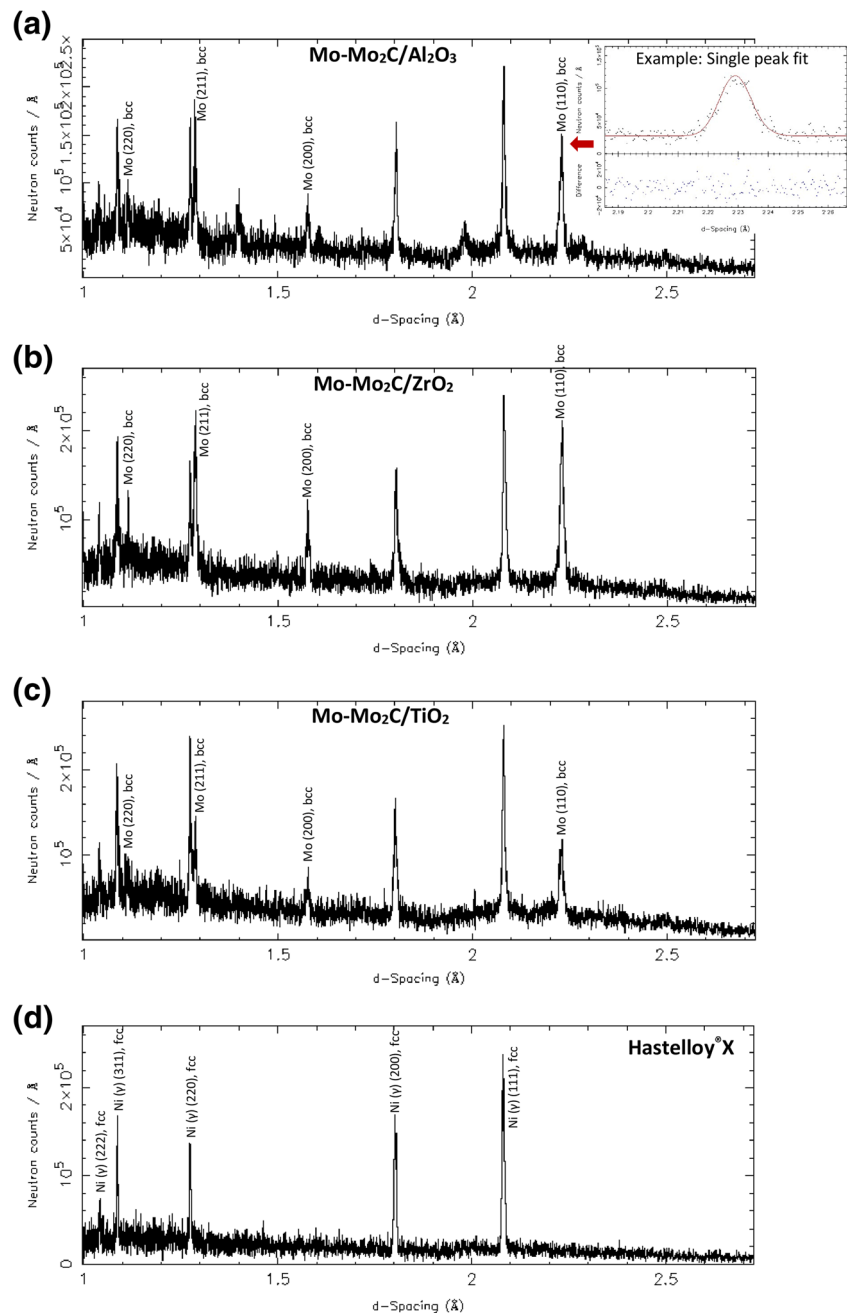
Fig. 4 Nanoindentation results on the cross-section of APS coated anode layer specimens (Mo-Mo₂C/Al₂O₃, Mo-Mo₂C/ZrO₂ and Mo-Mo₂C/TiO₂) on Hastelloy®X substrates: (a) hardness, (b) elastic modulus, and (c) SEM image showing five Berkovich nanoindentation residual impressions (along yellow line) on Hastelloy®X substrate near the coating-substrate interface (shown for Mo-Mo₂C/TiO₂ anode specimen)



Neutron Diffraction Measurements

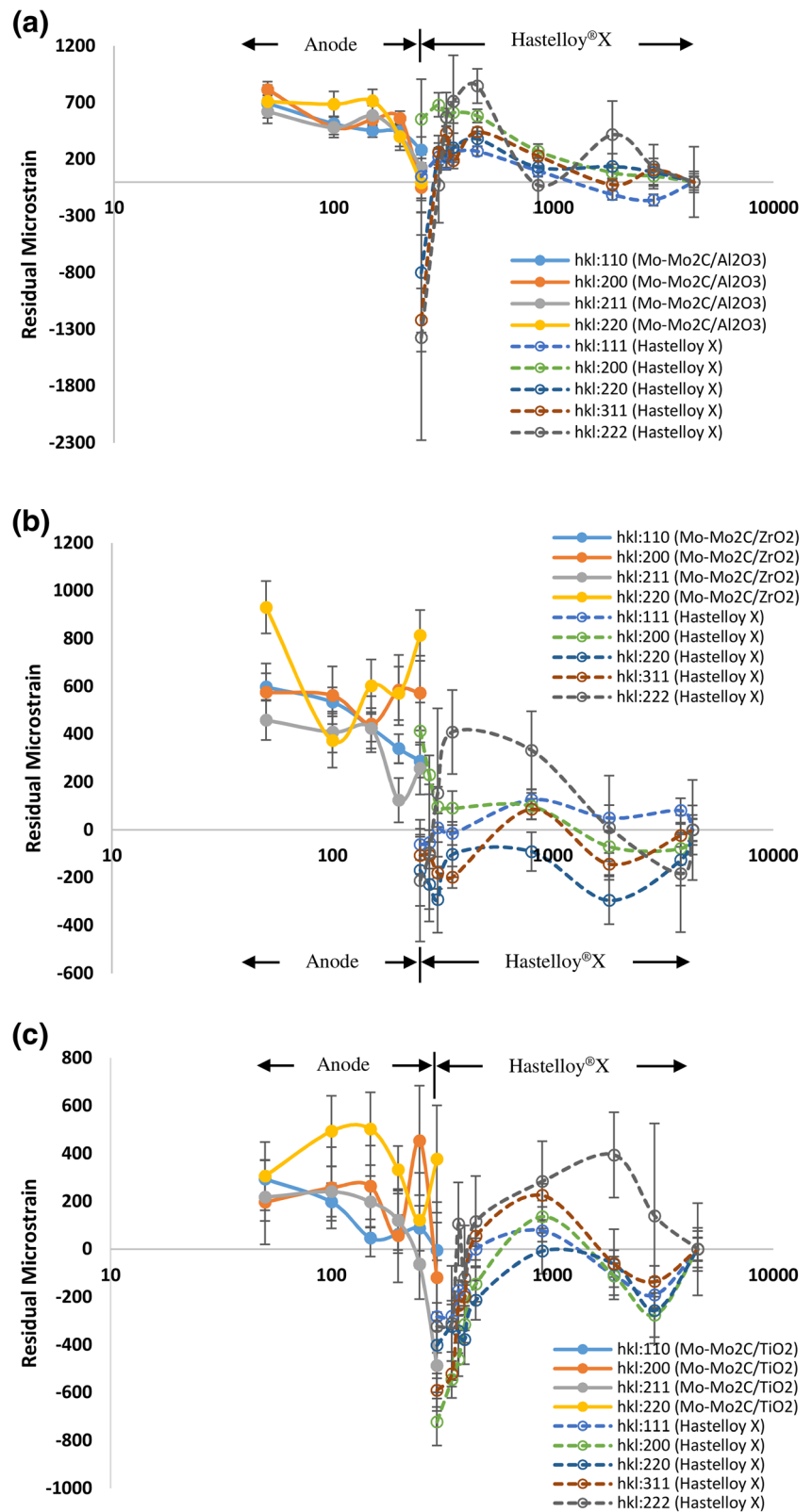
The Fig. 5 presents neutron diffraction patterns near the anode-substrate interface in the anode layer (also includes hkl peaks which were identified and analysed) for Mo-Mo₂C/Al₂O₃, Mo-Mo₂C/ZrO₂, and Mo-Mo₂C/TiO₂, and in the substrate Hastelloy®X of the anode Mo-Mo₂C/Al₂O₃ layer. It is important to note that the (hkl) peaks identified and analysed include four molybdenum (Mo) peaks (body-centred cubic or bcc) for each anode layers [(110), (200), (211) and (220)] and five Ni (gamma phase, is a face-centred cubic or fcc) peaks for each Hastelloy®X substrates [(111), (200), (220), (311) and (222)].

Fig. 5 Neutron diffraction pattern near the anode-substrate interface in the anode layer part (including hkl peaks identified and analysed): **(a)** Mo-Mo₂C/Al₂O₃, **(b)** Mo-Mo₂C/ZrO₂, **(c)** Mo-Mo₂C/TiO₂, and **d** Hastelloy®X substrate of anode Mo-Mo₂C/Al₂O₃ coating (used as d_{hkl}^0 for Hastelloy®X substrate); [Note: inset in **(a)** shows an example of single peak fit curve (pseudo-Voigt function)]



As shown in Fig. 6, the residual strain measurements were performed through thickness of specimens using a fully submerged gauge volume for deeper beam penetration and a partially submerged volume for near surface analysis [32–34]. Individual diffraction peaks corresponding to crystallographic planes (110), (200), (211) and (220) were employed to measure the average residual strain in each of the three anode layers, whereas, diffraction peaks corresponding to crystallographic planes (111), (200), (220), (311) and (222) were used to measure the average residual strain in the Hastelloy®X substrate. The x -axis of these plots was analysed on a logarithmic scale to highlight the variation in the anode-substrate strain.

Fig. 6 Single peak fitting routine analysis for neutron diffraction residual strain in anodes (for planes: (110), (220), (211), (220)) and 4.67 mm thick Hastelloy®X substrate (for planes: (111), (200), (220), (311), (222)): (a) Mo-Mo₂C/Al₂O₃ (250 μm thick), (b) Mo-Mo₂C/ZrO₂ (220 μm thick), and (c) Mo-Mo₂C/TiO₂ (300 μm thick)



The trends of residual strain in each of the three anode layers for diffraction peaks corresponding to crystallographic planes (110), (200), (211) and (220) were largely tensile with

some compression near the interface (e.g. in Mo-Mo₂C/TiO₂) for planes (211) and (200). The trends of residual strain in each of the three Hastelloy®X substrates for diffraction peaks

corresponding to crystallographic planes (111), (200), (220), (311) and (222) were highly compressive stress at the interface (except for plane (200) in Hastelloy®X substrates with Mo-Mo₂C/Al₂O₃, Mo-Mo₂C/ZrO₂ anode layers), including some relatively high tensile residual strain away from the interface in the Hastelloy®X substrate for plane (222).

While analysing the residual strain results obtained from an average of individual diffraction peaks, it can be seen that the trends of residual strain in each of the three anode layers for diffraction peaks corresponding to crystallographic planes (110), (200), (211) and (220) were mainly tensile (Fig. 7(a)). Results indicated that the average trends of residual strain in each of the three Hastelloy®X substrates for diffraction peaks corresponding to crystallographic planes (111), (200), (220), (311) and (222) were compressive at the interface, including some high tensile average residual strain away from the interface in the substrate, for example, for the Mo-Mo₂C/Al₂O₃ anode substrate. To convert the through thickness residual strain data to analyse the corresponding residual stress

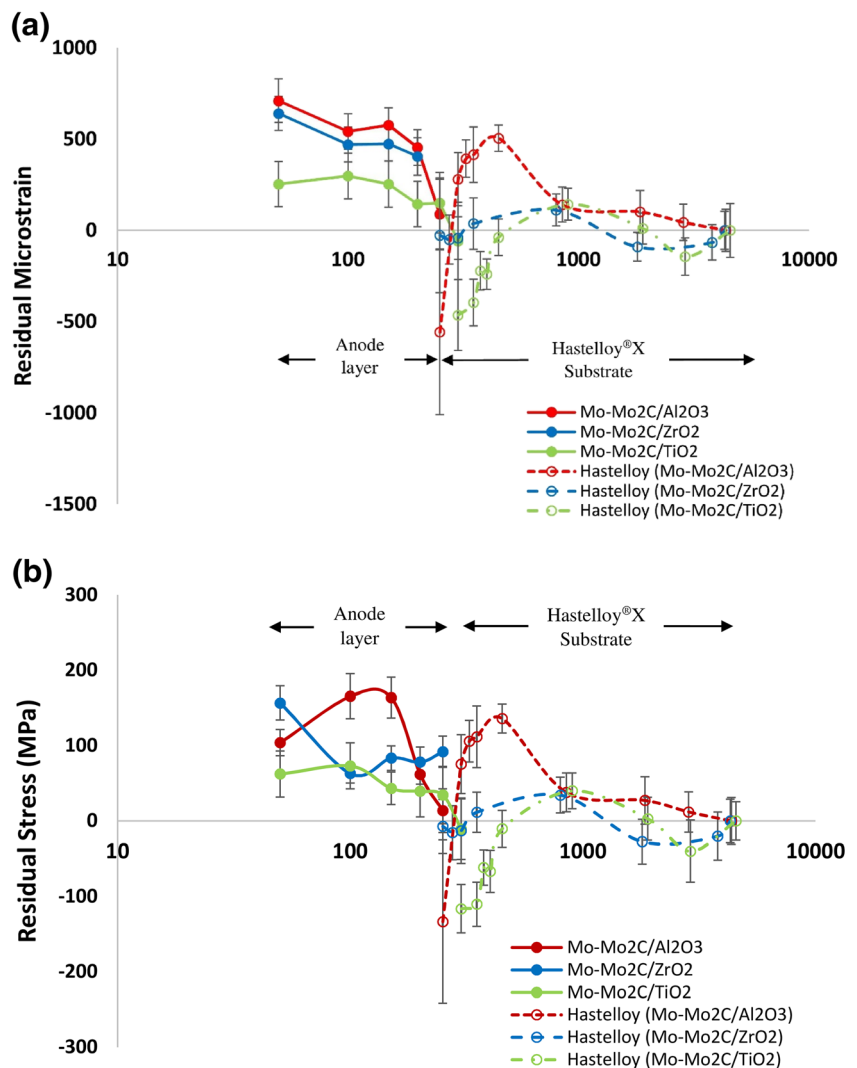
distribution (Fig. 7(b)), an average value of measured elastic modulus (Fig. 4) was utilized where measurement depth location of residual strain and elastic modulus did not match. This portion of the investigation indicated that the anode and substrate individual peaks or average residual strain/stress varied significantly with the anode coating conditions.

Discussion

Analysis of Anode Morphology and Nanoindentation Testing

As mentioned earlier, anode layers of 200 μm to 300 μm thicknesses and with a volumetric porosity as high as 20% could be produced by selecting the proper atmospheric plasma spray (APS) process parameters without the need for the addition of a pore-forming material. For example, Fig. 2(I) showed the coating's surface, which was mainly composed

Fig. 7 Neutron diffraction measurements and comparison: (a) residual strain comparison (based on average of all individual peak routine analysis) of plasma sprayed SOFC anodes on 4.76 mm thick Hastelloy®X substrates, and (b) corresponding residual stress [Mo-Mo₂C/Al₂O₃ (250 μm thick), Mo-Mo₂C/ZrO₂ (220 μm thick), Mo-Mo₂C/TiO₂ (300 μm thick)]



of splats with some semi- or partially-molten granules, including surface connected macro-pores and cracks in splats (but very little in Mo-Mo₂C/Al₂O₃, Fig. 2(I) (a)). This suggests that the pores formed as a result of reduced bonding between adjacent splats, while micro-cracking arose from contraction of the splat in the course of quenching and succeeding differential thermal contraction between substrate and coating. This confirms previous related results from our investigations [32–35]. For the anode cross-section surfaces (Fig. 2(II)), the splat thickness and features within appeared more or less very similar for all three anode layers (Mo-Mo₂C/Al₂O₃, Mo-Mo₂C/TiO₂ and Mo-Mo₂C/ZrO₂) with distinct layer gaps between splats (i.e. the splat does not appear to have dissolved). It can be argued that the slight variance in splat structures may be due to dissimilar powder shape and sizes.

In the XRD pattern, though the main phase was metallic molybdenum (Mo), considering some unique phase, as shown in Fig. 3 for the Mo-Mo₂C/Al₂O₃ anode layer, there was a small amount of aluminium-molybdenum-carbide (Al₂Mo₃C). Al₂Mo₃C is known to be a superconductor at a specific temperature as mentioned by Weil [45]. One can speculate that one possible area for further study is an SOFC coating as a superconductor.

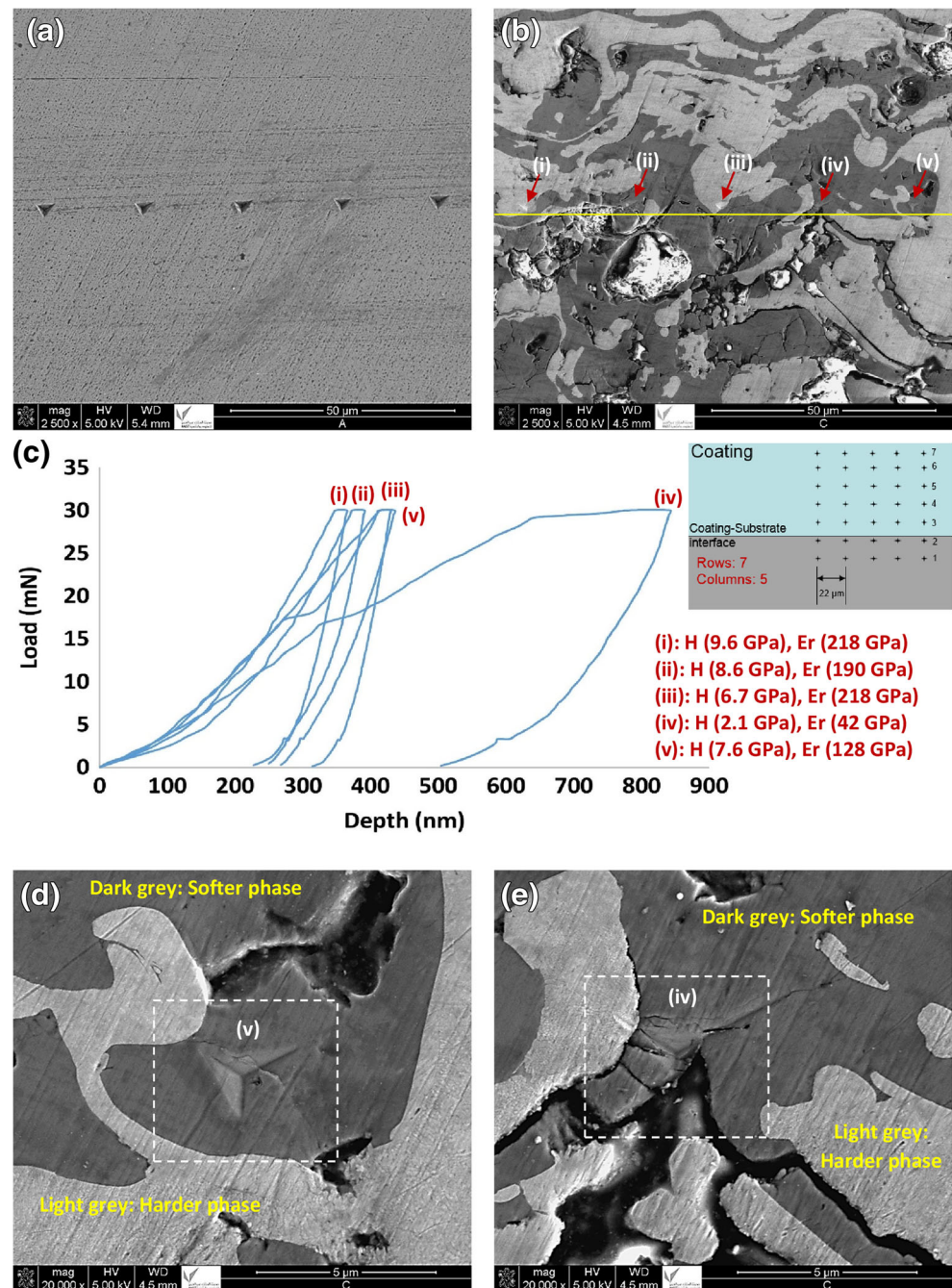
Overall hardness results indicated that the upper layers of the anode surface have higher average values than the subsurface layers in the anode layer with some effect of APS high temperature deposition on the substrate (i.e. higher bound at the interface for each specimens). The average hardness measured using nanoindentation technique for the anode layer cross-section surface (Fig. 4(a)) in the current investigation was found to lie within the range 5 GPa to 9 GPa (for Mo-Mo₂C/Al₂O₃ anode layer), 5 GPa and 10 GPa (for Mo-Mo₂C/ZrO₂ anode layer), 7 GPa and 14 GPa (for Mo-Mo₂C/TiO₂ anode layer), with a significantly high standard deviation within coating and low standard deviation in the substrate (Hastelloy®X). The small differences in the average hardness can be attributed to the lower degree of phase transformation in APS during deposition of Mo-Mo₂C/ZrO₂ and Mo-Mo₂C/TiO₂. This could also lead to potential differences between the measured elastic values. Other factors, such as inter-splat bonding, residual stress and porosity may also contribute to the differences in the elastic modulus of the three anode layer coatings. In addition, high standard deviations in through thickness nanoindentation measurements (i.e. hardness, elastic modulus) also suggest an important effect of the compound anode morphology (Fig. 4(b)). For example, the average elastic modulus measured for anode layer cross-section surface ranged between 283 GPa to 305 GPa (for Mo-Mo₂C/Al₂O₃ anode layer), 134 GPa and 244 GPa (for Mo-Mo₂C/ZrO₂ anode layer), 171 GPa and 275 GPa (for Mo-Mo₂C/TiO₂ anode layer), with a significantly high standard deviation in the coating zones and a low standard deviation in the substrate (Hastelloy®X) zones.

The complex anode coating cross-sectional morphology is best expressed in Fig. 8 which presents an example of Berkovich nanoindentation at 30 mN load for the anode cross-section in Mo-Mo₂C/TiO₂. Here the indent line shown in the Hastelloy®X substrate cross-section (i.e. 100 μm away from the coating-substrate interface in substrate, Fig. 8(a)), suggests a moderately uniform microstructure, leading to a low standard deviation in the substrate (Hastelloy®X) zones, as seen in Fig. 4. For the indent mark presented for the anode cross-section in Mo-Mo₂C/TiO₂ (220 μm away from the coating-substrate interface in coating, Fig. 8(b)), showing indentation of non-uniform microstructure (surface), leading to high standard deviation in anode zones, seen in Fig. 4. The Fig. 8(c) presents the corresponding *P-h* profiles for the anode cross-section in Mo-Mo₂C/TiO₂ including the inbox in *P-h* profiles which indicate that each anode coating forms distinct alternating layers of the two materials (identifiable largely by light grey and also by dark grey lamellar structures) in each anode coatings (e.g. Fig. 8(d, e) for Mo-Mo₂C/TiO₂). Also, evident from XRD pattern in Fig. 3 for Mo-Mo₂C/TiO₂ anode layer, the main phase by a considerable margin was lighter grey metallic molybdenum (Mo) including the high temperature polymorph of darker grey titania (TiO₂, rutile) was present. The Fig. 8(d) shows a zoomed view of Berkovich indentation for indent 5 (on darker phase with hardness (7.6 GPa), reduced elastic modulus (128 GPa)), and for a zoomed view of Berkovich indentation for indent 4 (on darker phase with impaired indenter landing). The indent 1 (on lighter grey phase) suggests higher hardness (9.6 GPa) and reduced elastic modulus (218 GPa) compared to the darker grey phase. The values for indent 4 (hardness = 2.1 GPa; reduced elastic modulus = 42 GPa) is much low possibly because it landed on the edge.

In the current investigation, the Poisson ratio for the anode layer was taken as 0.30 (Mo [37], due to dominant phase observed in X-ray and neutron diffraction), however, the elastic modulus values can be influenced by the Poisson's ratio (ν_s) of the specimen. Some references recommended a Poisson's ratio value as high as 0.32 for Mo [38]. From the present investigation, a sensitivity analysis indicated that the average modulus will change (i.e. decrease) by about 1.36% if a higher Poisson's ratio value of 0.32 is used. Considering the sensitivity of Mo₂C, Nino et al. [39] suggested a value of 0.28, which is very similar to the Poisson ratio for the Hastelloy [39], the average modulus will change (i.e. increase) by about 1.08%.

The APS spraying conditions appeared to have only a slight effect on the average modulus (Fig. 4(b)). Also, the higher magnification images of the Hastelloy®X substrate near the interface indicated negligible differences in the microstructure. The hardness did not show substantial differences between the near-interface hardness of the Hastelloy®X between the anode materials, indicating that

Fig. 8 Berkovich nanoindentation at 30 mN load: (a) indent line shown in Hastelloy®X substrate cross-section (100 μm away from the coating-substrate interface in substrate), and inset shows the scheme of indentation array, (b) indent line shown here for anode cross-section in Mo-Mo₂C/TiO₂ (220 μm away from the coating-substrate interface in coating), (c) corresponding P-h profiles of (b), (d) zoomed view of Berkovich indentation for indent 5, and (e) zoomed view of Berkovich indentation for indent 4



microstructural transformation was not substantial, which was consistent with the observed microstructure (Fig. 4(b)). Hence, it was difficult to relate this small change in modulus and no change in hardness of near coating-substrate interface modulus of Hastelloy®X on possible microstructural transformations in Hastelloy®X during APS coating deposition. As shown in Fig. 4(c), it possible that near interface nanoindentation may land in the gaps (non in this case) or either on the substrate or coatings and hence some results may have been related to coating and other to the substrate.

Assessment of Anode Residual Strain and Residual Stress Profiles

The residual strain and stress results (presented in Fig. 7) indicated that, with all other factors constant, the measured strain is dependent upon the depth of measurement. This in turn is suggestive of the combined effect of thermal mismatch based on the difference in the coefficient of thermal expansion (α_{CTE}) of the anode coating and substrate system, the role of quenching stress in individual lamellae, and the effect of phase transformations [32–34]. Furthermore, residual stress

measurement of the molybdenum (bcc) structure in Mo-Mo₂C/Al₂O₃ anode layer (for planes: (110), (220), (211), (220)) indicated largely tensile residual strains, whereas planes ((111), (200), (220), (311), (222)) in Hastelloy®X substrate which are Ni (gamma, are face-centred cubic or fcc) peaks indicating compressive strain values at the interface for all measured planes except (200) which was tensile strain throughout the substrate thickness. This dependency of measured values on the plane is not unusual on the basis of volume conservation and Poisson's ratio. However, it does indicate that when a single peak fitting analysis is used (e.g. in the $\sin^2\psi$ technique in X-ray measurements), the results will be sensitive to the designated peak, and hence reported stress values are not uncommon, indicating not only the difficulty of residual strain measurement in these complex materials but also that the multiple peak through thickness analysis via neutron diffraction provides a more detailed strain analysis.

As summarised above in “Assessing Neutron Diffraction Residual Strain” section, the strain was obtained from the shift in individual peaks for the coating and substrate materials obtained using a single-peak fitting. Single-peak fits use a peak profile consisting of the convolution of a truncated exponential with a pseudo-Voigt function (note: pseudo-Voigt part is a convolution of Gaussian and Lorentzian curves) shown in Fig. 5(a) routine. The quality of single peak fitting to the neutron diffraction is shown in the zoomed window for the Mo (110 bcc) peak in Fig. 5(a) which has resulted in standard deviations of strain measurements (Fig. 7) which are consistent with previous studies on thermal spray coatings [e.g. 32–35].

In general, for simple crystal structures Rietveld refinement analysis can be applied which considers multiple peaks in the spectra to evaluate lattice parameters. However, Rietveld refinement can be difficult to apply where the spectra has overlapping peaks. In the current study overlapping peaks are possible due to submergence of the beam in both coating and substrate materials and formation of other compounds, which reduces the reliability of Rietveld refinement. As the Mo peak in the current study had no overlapping peaks (Figs. 3 and 5), a single peak fitting refinement was used, which is consistent with previous studies of thermal spray coatings [32–35]. At Engin-X neutron scattering facility, peak positions can be precisely determined by “least-squares” refinement of the peaks, with a typical sensitivity of $50 \mu\epsilon$ ($1 \mu\epsilon = 10^{-6}$). Least-squares means that the overall solution minimizes the sum of the squares of the errors made in the results of every single equation. Each diffraction peak provides information from only a small fraction of the crystallites within the sampled volume, i.e. those oriented to fulfil the Bragg condition. As summarised by Santisteban et al. [46], a good approximation to the macroscopic (engineering) elastic strain is usually given by a weighted average of several single-peak strains (ϵ_{hkl}). In such time-of-flight (TOF) based neutron scattering

instruments, the engineering strain can also be approximated from the change in the average lattice parameters from Rietveld or Pawley refinements of the complete diffraction spectrum.

The neutron scattering for strain measurement is conceptually very simple but its practical application can be time-consuming. Very long counting times are required when small gauge volumes and large penetration depths are involved [46]. In the current investigation, large counting times for coatings and in substrate near interface (3 h per vertical depth) and short counting times for substrates away from interface (1 h per vertical depth) were used to ensure data quality.

Surface properties (e.g. texture) in thermal spray coatings can originate from quenching of lamellae and plastic deformation of un-molten coating particles [32, 47]. Thermo-mechanical characteristics of anode particles during deposition therefore control the degree of texturing in thermal spray coatings. The analysis of multiple peaks presented in this investigation (Fig. 6(a)) therefore highlights this dependency of texture, which can form during coating formation in APS, on residual strain. This anode texturing and its influence on residual strain will also influence its thermo-mechanical performance, which will improve in grains that are oriented such that they carry a compressive residual strain near anode layer/substrate interface.

For bulk (macro) mechanical property evaluations, an averaged value of strain, e.g. as indicated in Fig. 7 can be used to interpret the macro-strain in the anode specimens. Such detailed strain analysis is currently not possible using other techniques e.g. $\sin^2\psi$ where a single peak is measured or hole-drilling or curvature techniques where an averaged stress is estimated. Even for neutron based residual strain measurements, complications do arise. For example, the gauge volume contains diffraction peaks from both the coating and substrate materials, which overlap and reduce the accuracy of Rietveld peak refinement [32–34].

As was seen in Fig. 7, the measurements of the average residual strain/stress profile in the anode layer varied significantly with the coating conditions. The average residual strain and residual stress in the Mo-Mo₂C/Al₂O₃ anode layer and Mo-Mo₂C/TiO₂ anode layer changed from tensile near the surface to compressive at the interface, whereas the average residual strain/stress in the Mo-Mo₂C/ZrO₂ anode layer was slightly tensile. These residual strain values revealed the collective outcome of a thermal mismatch founded on the dissimilarity in the coefficient of thermal expansion (α_{CTE}) of the anode layer/substrate system, the role of quenching stress in specific lamellae, and the influence of phase changes [32–34]. These factors have been discussed in detail by Ahmed et al. [32] on the basis of physical mechanisms dictating the residual stress behaviour. Additionally, residual stresses within a coating can disturb the coating bond on a substrate, predominantly for cyclical temperature operation [48], especially in SOFC. It

can be argued that the reduction of the residual stress and enhanced bonding between the anode layers should diminish the trend to delaminate, especially during thermal cycling in fuel cell operation.

Comparison with the coefficient of thermal expansion model

Estimates of the macro-residual stresses due to thermal expansion mismatch in a two-layer system can be based on equation (2) assuming that the linear coefficient of thermal expansion (CTE) does not vary within ΔT [48, 49]:

$$\sigma_A = \frac{1}{d_A} \cdot \left(\frac{(\alpha_B - \alpha_A) \cdot \Delta T}{\frac{1 - \nu_A}{d_A \cdot E_A} + \frac{1 - \nu_B}{d_B \cdot E_B}} \right) \quad (2)$$

where σ , E , ν , α and ΔT are the thermal stress, elastic modulus, Poisson's ratio, CTE, and the temperature change, respectively (see Tables 2 and 3) [50, 51]. In the equation (2), the subscripts "A" and "B" refer to the anode layer coating and the substrate, respectively. It is known that the particle temperature upon impact during air plasma spraying can be around 1873 ± 473 K [52].

Thermal stress which was calculated using equation (2) with a temperature change, $\Delta T = 1573$ K and assumed cooling to room temperature, 300 K, and CTE values from Table 2, were consistent with the averaged residual tensile strain and stress values in the anode layers and the averaged residual compressive strain and stress values in the substrate near interface (Fig. 7 and Table 3). It can be reasoned that thermal stress and strain values calculated by equation (2) however may not be accurate as it assumes perfect (i.e. defect free) bonding at the anode layer/substrate interface [53, 54]. Phase changes are also not considered. Moreover, the neutron diffraction analysis evaluated the strain in the molybdenum crystals which formed most of the anode layer. The atomic percent of Mo was however relatively low at 45%. Hence the strain in the Mo crystal will be effected by the CTE value

difference between Mo (5.3×10^{-6} (20 °C)) and Mo₂C (7.8×10^{-6} (20 °C)) and other constituents such as Al₂O₃ (5.5×10^{-6} (20 °C)), ZrO₂ (7.0×10^{-6} (20 °C)), TiO₂ (7.1×10^{-6} (20 °C)), as shown in Table 2. Therefore, there is strain in Mo caused by the CTE difference between the coating and substrate material and the CTE difference amongst the crystalline phases of the layer. These variances, in addition to the quenching stresses will lead to a diverse assessment between the stress values calculated from equation (2) and the neutron scattering results. As the coating composition is largely Mo, the neutron scattering analysis of Mo peaks can be assumed to represent the overall stress state of the coating.

The quenching stress, which appears within different splats, is caused by constrained contraction of the solidifying splat during cooling process, since its shrinkage is inhibited by the underlying lamella. This again is a function of the temperature of individually sprayed splats. As previously mentioned [2, 34], quenching stress is always tensile, while thermal mismatch stress can be tensile or compressive. The tensile nature of the residual stress suggests that the quenching stress component is larger than the thermal mismatch stress factor. This outcome is likely partially due to the great variances amongst the coefficient of thermal expansion (CTE) of each component in the anode layers and the substrate (Table 3). As indicated in Fig. 3, there was a higher degree of crystallinity in each of the anode layers. Although the influence of these transformations is appreciable between different planes of strain measurement (Fig. 7), when compared to the differences between the Mo-Mo₂C/Al₂O₃, Mo-Mo₂C/ZrO₂ anode, and the Mo-Mo₂C/TiO₂ anode specimens, the overall influence on the averaged strain and stress values (Fig. 7) is minor.

Influence of coating morphology

Two types of microstructural flaws were found to be present in the materials: micro-cracks (i.e. very little in Mo-Mo₂C/Al₂O₃, to almost none in Mo-Mo₂C/ZrO₂ and Mo-Mo₂C/TiO₂), and pores, as indicated by arrows in Fig. 2. The extent to which both defect types occur can be changed (i.e. enhanced/reduced)

Table 2 Materials properties

Material	α_{CTE} (K ⁻¹)	Elastic modulus (GPa)	Tensile strength (MPa)	Hardness (GPa)	Melting temperature (°C)	Ref.
Mo	5.3×10^{-6} (20 °C)	330	324	2.2	2617	[46]
Mo ₂ C	7.8×10^{-6} (20 °C)	227–553	Not available	19	2505–2692	[46]
Mo-Mo ₂ C	Not available	Not available	Not available	Not available	2620	Metco 64
Al ₂ O ₃	5.5×10^{-6} (20 °C)	215–413	300	5.5–22.0	2054	[46, 47]
ZrO ₂	7.0×10^{-6} (20 °C)	100–250	711	5.5–15.7	2700	[46, 47]
TiO ₂	7.1×10^{-6} (20 °C)	230–288	367	9.3–10.2	1843	[46, 47]
Hastelloy®X	13.8×10^{-6} (25–300 °C)	205	245	3.6–3.8 (current measurement)	1260–1355	[39, 47]



Table 3 Thermal stress and strain calculations (using analytical method) for anode layer and substrate

Type	Material	Elastic modulus (GPa), [average measured value from nanoindentation]	Poisson's ratio, ν	Layer thickness (μm), d	α_{CTE} (K^{-1})	*Calculated thermal stress (MPa) (+ve: tensile; -ve: compressive)	Calculated thermal strain ($(\alpha_B - \alpha_A) \cdot \Delta T$, micro strain)
#1	Mo-Mo ₂ C/Al ₂ O ₃	$E_A = 205$	ν_A (Mo) = 0.30 ν_A (Mo ₂ C) = 0.24	$d_A = 250$	Mo: 5.3×10^{-6} Mo ₂ C: 7.8×10^{-6}	+3761 with Mo +2453 with Mo ₂ C	+13,370 with Mo +9438 with Mo ₂ C
	Hastelloy@X	$E_B = 255$	$\nu_B = 0.32$	$d_B = 4760$	Hastelloy@X: 13.8×10^{-6}	-197 with Mo -128 with Mo ₂ C	-13,370 with Mo -9438 with Mo ₂ C
#2	Mo-Mo ₂ C/ZrO ₂	$E_A = 188$	ν_A (Mo) = 0.30 ν_A (Mo ₂ C) = 0.24	$d_A = 220$	Mo: 5.3×10^{-6} Mo ₂ C: 7.8×10^{-6}	3488 with Mo +2273 with Mo ₂ C	+13,370 with Mo +9438 with Mo ₂ C
	Hastelloy@X	$E_B = 288$	$\nu_B = 0.32$	$d_B = 4760$	Hastelloy@X: 13.8×10^{-6}	-161 with Mo -105 with Mo ₂ C	-13,370 with Mo -9438 with Mo ₂ C
#3	Mo-Mo ₂ C/TiO ₂	$E_A = 222$	ν_A (Mo) = 0.30 ν_A (Mo ₂ C) = 0.24	$d_A = 300$	Mo: 5.3×10^{-6} Mo ₂ C: 7.8×10^{-6}	+4033 with Mo +2632 with Mo ₂ C	+13,370 with Mo +9438 with Mo ₂ C
	Hastelloy@X	$E_B = 265$	$\nu_B = 0.32$	$d_B = 4760$	Hastelloy@X: 13.8×10^{-6}	-254 with Mo -165 with Mo ₂ C	-13,370 with Mo -9438 with Mo ₂ C

(*Thermal stress was calculated using equation (2) with $\Delta T = 1573$ K and CTE values while considering Mo and Mo₂C as bulk anode layer from Table 3, A = Coating, B = Substrate)

by modifying thermal spraying processing parameters and powder composition. Micro-cracks are generated during quenching of the molten splats to relieve the tensile stresses [2] and are undesirable. On the other hand, pores are formed by a number of mechanisms (e.g. incomplete penetration of molten splats into surface crevices and the inclusion of partially melted particles in the coating [55]) need to be controlled to improve the efficiency of the SOFC. Cracks which can run through most or all of the anode layer thicknesses can form to relieve tensile stress. Micro-cracks and pores relax stresses locally, while the other cracks provide stress relief for larger sections of the anode layers. Both of these features i.e. cracks and pores reduce the mechanical integrity of the SOFC. Likewise, it is important to note that fissures provide good stress relief in the anode layers, resulting in residual stress levels in the anode layers that are smaller (Fig. 7(b)) than the tensile strength of bulk molybdenum (324 MPa [50, 51], and not necessarily thermally sprayed Mo coatings), including other materials in the anode composition (Table 3).

Comparison with previous studies

A comparison (i.e. only three literature papers could be found) of published literature on the residual stress values of thermally sprayed electrodes in SOFC indicated that the residual stress values are very much dependent upon the material and the measurement methods (Table 4). The X-ray diffraction values of measured residual stress using the $\sin^2\psi$ technique for SOFC electrodes indicated that the stress is always tensile or compressive at the coating surface (Table 4) depending upon the coating substrate combination. As discussed earlier, this is inconsistent with the mechanisms of residual stress generation on the basis of the coefficient of thermal expansion (CTE) difference and also the role of quenching stresses (and can also depend on the X-ray beam penetration depth of measurements, about 6 μm reported by Heimann et al. [56]). The values quoted from the synchrotron X-ray method largely indicated very high compressive residual stress values (between -0.59 GPa to -2.1 GPa) varying through the plasma sprayed anode layer thickness (e.g. [4]). Similarly, the measured strains in the plasma-sprayed NiO/LDC anode layer on Ni substrate (with LSCM buffer) were in compressive states, with no obvious differences of residual strains between the specimens with various coating thicknesses of NiO/LDC [5]. However, the compressive residual strain in the NiO/LDC anode layer coating can be reduced with increasing substrate temperature during the plasma spraying. It has been reported that the higher compressive residual strain can lessen the bonding strength between coating and substrate [4, 5]. Therefore, the heating of the substrate in the course of plasma spraying is a significant issue for achieving good mechanical stability of the NiO/LDC anode on the porous Ni substrate for SOFC [5].

Table 4 Literature results of residual stress in thermally sprayed solid oxide fuel cell (SOFC)

Residual stress measurement method	Coating process	Electrode thickness (μm)	Elastic modulus (E , GPa)	Crystal plane (hkl)	Substrate details	Residual stress values (σ_R , MPa) (+): tensile (-): compressive	Comments on residual stress profile of coating and substrate	Ref.
X-ray diffraction	SPS	Electrolyte (yttria-stabilized zirconia, YSZ), 80 μm	$E_{(631)} = 242$ at room temperature	Cubic YSZ (531)	LSM/YSZ + MG 2 (media grade) substrates consisted of 40 μm thick cathode layers on porous 430 stainless steel discs (25.4 mm dia., 1.6 mm thick)	+35 to +91 MPa	Residual stress decreased to 39 MPa when the temperature was increased from room temperature to 750 $^{\circ}\text{C}$	[2]
X-ray diffraction (synchrotron radiation)	APS	Anode NiO/LDC; Thicknesses: S1: 5 μm , S2: 12 μm , S3: 20 μm , S4–S7: 12 μm [LDC (Ce _{0.55} La _{0.45} O ₃ - δ)]	$E = 217$ GPa and Poisson's ratio $\nu = 0.33$ of GDC (due to the absence of the theoretical E of LDC)	Cubic fluorite La doped CeO ₂ (311)	Porous Ni (1 mm thickness, 24 mm dia.)	S1: 5 μm /515 $^{\circ}\text{C}$ /-1.37 GPa; S2: 12 μm /515 $^{\circ}\text{C}$ /-1.22 GPa; S3: 20 μm /515 $^{\circ}\text{C}$ /-1.32 GPa; S4: 12 μm /27 $^{\circ}\text{C}$ /-2.10 GPa; S5: 12 μm /288 $^{\circ}\text{C}$ /-1.87 GPa; S6: 12 μm /554 $^{\circ}\text{C}$ /-1.26 GPa; S7: 12 μm /606 $^{\circ}\text{C}$ /-0.59 GPa.	Biaxial state of residual stresses at 0 $^{\circ}$, 45 $^{\circ}$ and 90 $^{\circ}$ with respect to the spraying direction. The residual stresses at 0 $^{\circ}$, 45 $^{\circ}$ and 90 $^{\circ}$ with respect to the spraying direction (i.e. σ_{θ} , $\sigma_{45^{\circ}}$, $\sigma_{90^{\circ}}$) for the NiO/LDC anode coatings were all compressive	[4]
X-ray diffraction (synchrotron radiation)	APS	Cathode: LSGM/LSCF and LSCF; Electrolyte: - LSGM; Interlayer between electrolyte and anode: LDC; Anode: NiO/LDC anode + LSCM buffer on Ni substrate; LSCM (La _{0.75} Sr _{0.25} Cr _{0.5} Mn _{0.5} O ₃ - δ), LDC (Ce _{0.55} La _{0.45} O ₃ - δ), LSGM (La _{0.85} Sr _{0.2} Ga _{0.8} Mg _{0.2} O ₃ - δ), LSCF (La _{0.58} Sr _{0.4} Co _{0.2} Fe _{0.8} O ₃ - δ).		-	Porous Ni (size: 100 mm (l) \times 10 mm(w) \times 1 mm(t))	Residual strains, % (as-sprayed) -0.48 (LSGM); Surface side -0.27 (NiO); Buffer side -0.79 (NiO); Surface side -0.32 (LDC); Anode side -1.48 (LDC); -0.46 (NiO); -0.72 (LSGM); -0.59 (LSCF);	As-sprayed test strip presents compressive residual strain. The test strip reveals compressive residual strain in cooling process. LSCM buffer reverses into tensile residual strain if it is sprayed with an anode coating.	[5]



Residual stress and durability of SOFCs

Neutron diffraction due to its high beam penetration, unlike other measurement techniques (e.g. X-ray synchrotron radiation [2, 19, 20, 57]), offers the opportunity to non-destructively measure the through thickness stress profile. It is also important to note that there is no well-established model for the relationships between anode layer degradation, failure and total stress distribution during usage of SOFC at high temperatures. Since the SOFC electrodes can degrade faster at elevated temperature or those subjected to higher levels of loading, the combined loading stress during operation and pre-existing residual stress in electrodes can significantly affect the response of the overall electrode materials. Considering a similar level of loading during fuel cell operation, the magnitude and nature of pre-existing residual tensile stress in the SOFC system is expected to impact the electrode (i.e. anode, electrolyte, and cathode) degradation and failure with time. Nevertheless, thermal spraying such as air plasma spray is an important manufacturing method for SOFCs because it permits direct deposition of the functional anode layers on metal supports and may offer cost advantages over conventional manufacturing method [2, 4, 5]. The primary significance of this study is that it will aid in the electrode development process by providing practical information about thermo-mechanical properties such as flexural strength, fracture toughness and adhesion strength.

Conclusions

Anode layers of thicknesses between 200 μm to 300 μm and with porosities as high as 20% for Mo-Mo₂C/Al₂O₃ (250 μm thick layer) and Mo-Mo₂C/TiO₂ (300 μm thick layer) and around 17% for Mo-Mo₂C/ZrO₂ (220 μm thick layer), can be obtained in a controllable manner by selection appropriate air plasma spray (APS) process parameters without the need for addition of pore-forming material. The process parameters developed and structural analysis performed through the current work have paved the way for further development of other composite layers for a complete solid oxide fuel cell (SOFC). The following conclusions can be drawn:

- a. The through thickness residual stress profiles in the anode layers (Mo-Mo₂C/Al₂O₃, Mo-Mo₂C/ZrO₂ anode, and Mo-Mo₂C/TiO₂ specimens) were mainly tensile, being lowest at the interface with the substrate.
- b. Comparison of the residual average strain (and stress) profile indicated that the average tensile residual strain (and stress) in the Mo-Mo₂C/TiO₂ anode is the lowest, with the possible effect of metal oxide particle size and shape.
- c. The measured values of residual strain were not sensitive to the plane of strain measurement which explains the small influence of metal oxides in the anode layers.

- d. Anode layer residual stress affects microstructure conditions and nanoindentation based hardness results point to the upper layers of the anodes having higher values than the subsurface layers with some effect of the deposition on the substrate.

Acknowledgements The authors acknowledge the award of ENGIN-X beam time at the STFC ISIS Facility (experiment number RB1510283, April 2015) for the neutron diffraction measurements. Research funding was provided by Saudi Aramco (Contract number 6000074197) for anode development. We would also like to acknowledge the support of Youssef Elakwah (Alfaisal University, Saudi Arabia) for the assistance in nanoindentation tests and microscopic imaging.

Open Access This article is distributed under the terms of the Creative Commons Attribution 4.0 International License (<http://creativecommons.org/licenses/by/4.0/>), which permits unrestricted use, distribution, and reproduction in any medium, provided you give appropriate credit to the original author(s) and the source, provide a link to the Creative Commons license, and indicate if changes were made.

References

1. Shao Z, Haile SM, Ahn J, Ronney PD, Zhan Z, Barnett SA (2005) A thermally self-sustained micro solid-oxide fuel-cell stack with high power density. *Nature* 435:795–798
2. Macwan A, Chen DL, Marr M, Kesler O (2013) Residual stresses in suspension plasma sprayed electrolytes in metal-supported solid oxide fuel cell half cells. *J Power Sources* 221:397–405
3. Haile SM (2003) Fuel cell materials and components. *Acta Mater* 51:5981–6000
4. Yang YC, Lu LY, Hwang CS, Tsai CH (2013) Residual stresses in the atmospheric plasma sprayed NiO/LDC anode of the metallic supported solid oxide fuel cells. *Surface & Coatings Technology*. 231:193–200
5. Yang YC, Hwang CS, Tsai CH (2013) Evaluations of the residual strains in the plasma sprayed multi-layer electrodes of the solid oxide fuel cell. *Surf Coat Technol* 237:341–348
6. Yakabe H, Baba Y, Sakurai T, Yoshitaka Y (2004) Evaluation of the residual stress for anode-supported SOFCs. *J Power Sources* 135:9–16
7. Villanova J, Sicardy O, Fortunier R, Micha JS, Bleuet P (2010) Determination of global and local residual stresses in SOFC by X-ray diffraction. *Nucl Inst Methods Phys Res B* 268:282–286
8. Somekawa T, Fujita K, Matsuzaki Y (2013) Residual stress change with time of a segmented-in-series solid oxide fuel cell using an in situ X-ray stress measuring method. *J Power Sources* 221:64–69
9. Xiao Q, He H, Shao S, Shao J, Fan Z (2009) Influences of deposition rate and oxygen partial pressure on residual stress and microstructure of YSZ thin films. *Thin Solid Films* 517:4295–4298
10. Yeh TH, Lin RD, Cherng JS (2015) Effects of residual stress and interface dislocations on the ionic conductivity of yttria stabilized zirconia nano-films. *Thin Solid Films* 574:66–70
11. Schoderböck P, Brechbühl J (2015) Application of the whole powder pattern decomposition procedure in the residual stress analysis of layers and coatings. *Thin Solid Films* 589:419–426
12. Huang K, Harter HD (2010) Temperature-dependent residual stresses in plasma sprayed electrolyte thin-film on the cathode substrate of a solid oxide fuel cell. *Solid State Ionics* 181:943–946
13. Li N, Xiao J, Prudhomme N, Chen Z, Ji V (2014) Residual stresses in oxide scale formed on Fe–17Cr stainless steel. *Appl Surf Sci* 316: 108–113

14. Fischer W, Malzbender J, Blass G, Steinbrech RW (2005) Residual stresses in planar solid oxide fuel cells. *J Power Sources* 150:73–77
15. Malzbender J, Fischer W, Steinbrech RW (2008) Studies of residual stresses in planar solid oxide fuel cells. *J Power Sources* 182:594–598
16. Fujita K, Somekawa T, Hatae T, Matsuzaki Y (2011) Residual stress and redox cycling of segmented-in-series solid oxide fuel cells. *J Power Sources* 196:9022–9026
17. Charlas, B., Chatzichristodoulou, C., Brodersen, K., Kwok, K., Norby, P., Chen, M., Frandsen, H.L., 2014. Residual stresses in a co-sintered SOC half-cell during post-sintering cooling. In proceedings of 11th European SOFC and SOE forum. [B1107] European fuel cell Forum
18. Yakabe H, Baba Y, Sakurai T, Satoh M, Hirotsawa I, Yoda Y (2004) Evaluation of residual stresses in a SOFC stack. *J Power Sources* 131:278–284
19. Kimura, H., Sakaue, T., Akiniwa, Y., Tanaka, K., Yokoyama, M., Nagai, K., Shimano, J., Hisada, K., 2007. In situ measurement of internal stress in solid oxide fuel cell by synchrotron radiation. Proc. international symposium on ecotopia science. ISETS07, 184–188
20. Tanaka K, Akiniwa Y, Kimura H, Ukai K, Yokoyama M, Mizutani Y (2008) In situ synchrotron measurement of internal stresses in solid-oxide fuel cell during red-ox cycle. *Mater Sci Forum* 571-572: 339–344
21. López R, Comesaña R, del Val J, Durán A, Justo VM, Serbena FC, Pascual MJ (2015) Laser cladding of glass-ceramic sealants for SOFC. *J Eur Ceram Soc* 35:4475–4484
22. He CR, Wang WG, Wang J, Xue Y (2011) Effect of alumina on the curvature, Young's modulus, thermal expansion coefficient and residual stress of planar solid oxide fuel cells. *J Power Sources* 196: 7639–7644
23. Charlas B, Frandsen HL, Brodersen K, Henriksen PV, Chen M (2015) Residual stresses and strength of multilayer tape cast solid oxide fuel and electrolysis half-cells. *J Power Sources* 288:243–252
24. Atkinson A, Selcuk A (1999) Residual stress and fracture of laminated ceramic membranes. *Acta Mater* 47:867–874
25. Evans A, Prestat M, Tölke R, Schlupp MVF, Gauckler LJ, Safa Y, Hocker T, Courbat J, Briand D, de Rooij NF, Courty D (2012) Residual stress and buckling patterns of free-standing yttria-stabilized-zirconia membranes fabricated by pulsed laser deposition. *Fuel Cells* 12:614–623
26. Xiang, Z., Haibo, S., Fenghui, W., Kang, L., Jianye, H., 2014. Curvature reversal and residual stress in solid oxide fuel cell induced by chemical shrinkage and expansion. *Fuel Cells* 14:1057–1061
27. Clague R, Marquis AJ, Brandon NP (2012) Finite element and analytical stress analysis of a solid oxide fuel cell. *J Power Sources* 210:224–232
28. Zhao X, Wang F (2013) Elastoplastic properties of solid oxide fuel cell before and after reduction. *Acta Metall Sin (Engl Lett)* 26:137–142
29. Delette G, Laurencin J, Murer S, Leguillon D (2012) Effect of residual stresses on the propagation of interface cracks between dissimilar brittle materials: contribution of two and three-dimensional analyses. *Eur J Mech A Solids* 35:97–110
30. Malzbender J, Gestel TV (2013) Residual stress assessment for thin 8YSZ electrolytes using focused ion beam milling and digital image correlation. *Fuel Cells* 13:1076–1079
31. Chen Y, Yang L, Ren F, An K (2014) Visualizing the structural evolution of LSM/xYSZ composite cathodes for SOFC by in-situ neutron diffraction. *Sci Rep* 4(5179):1–9
32. Ahmed R, Faisal NH, Paradowska AM, Fitzpatrick M, Khor KA (2011) Neutron diffraction residual strain measurements in nanostructured hydroxyapatite coatings for orthopaedic implants. *J Mech Behav Biomed Mater* 4:2043–2054
33. Ahmed R, Faisal NH, Paradowska AM, Fitzpatrick M (2012) Residual strain and fracture response of Al₂O₃ coatings deposited via APS and HVOF techniques. *J Therm Spray Technol* 21:23–40
34. Ahmed R, Yu H, Stoica V, Edwards L, Santisteban JR (2008) Neutron diffraction residual strain measurements in post-treated thermal spray cermet coatings. *Mater Sci Eng A* 498:191–202
35. Faisal NH, Ahmed R, Katikaneni SP, Souentie S, Goosen MFA (2015) Development of plasma sprayed molybdenum carbide-based anode layers with various metal oxide precursors for SOFC. *J Therm Spray Technol* 24:1415–1428
36. Oliver WC, Pharr GM (1992) An improved technique for determining hardness and elastic modulus using load and displacement sensing indentation experiments. *J Mater Res* 7:1564–1583
37. Molybdenum Poisson's ratio; http://www.engineersedge.com/materials/poissons_ratio_metals_materials_chart_13160.htm (accessed 9 January 2016)
38. Molybdenum Poisson's ratio; http://www.engineeringtoolbox.com/metals-poissons-ratio-d_1268.html (accessed 9 January 2016)
39. Hastelloy® X alloy: Haynes International, Inc., Indiana, USA, 1997
40. Withers PJ, Johnson MW, Wright JS (2000) Neutron strain scanning using a radially collimated diffracted beam. *Physica B* 292: 273–285
41. Ganguly S, Stelmukh V, Edwards L, Fitzpatrick ME (2008) Analysis of residual stress in metal-inert-gas-welded Al-2024 using neutron and synchrotron X-ray diffraction. *Mater Sci Eng A* 491: 248–257
42. Ahmed R, Faisal NH, Al-Anazi NM, Al-Mutairi S, Toma F-L, Berger L-M, Potthoff A, Elakwah YO, Goosen MFA (2015) Structure property relationship of suspension thermally sprayed WC-Co nanocomposite coatings. *J Therm Spray Technol* 24(3): 357–377
43. Ahmed R, Ali O, Faisal NH, Al-Anazi NM, Al-Mutairi S, Toma F-L, Berger L-M, Potthoff A, Goosen MFA (2015) Sliding wear investigation of suspension sprayed WC-Co nanocomposite coatings. *Wear* 322-323:133–150
44. Ali O, Ahmed R, Faisal NH, Al-Anazi NM, Berger L-M, Kaiser A, Toma F-L, Polychroniadis EK, Sall M, Elakwah YO, Goosen MFA (2017) Influence of post-treatment on the microstructural and tribomechanical properties of suspension thermally sprayed WC-12 wt%Co nanocomposite coatings. *Tribol Lett* 65:33
45. Weil KS (1998) Analysis of the structure and magnetic properties of new multicomponent transition metal nitride compounds. *Electrochem Soc Interface Winter*:49–51
46. Santisteban JR, Daymond MR, James JA, Edwards L (2006) ENGIN-X: a third-generation neutron strain scanner. *J Appl Crystallogr* 39:812–825
47. Iordanova I, Forcey KS (1997) Texture and residual stresses in thermally sprayed coatings. *Surf Coat Technol* 91:174–182
48. McGinnis, A.J., Watkins, T.R., Jagannadham, K., 1999. Residual stresses in a multilayer system of coatings. Denver X-ray conference (DXC) on applications of X-ray analysis, International Centre for Diffraction Data (ICDD), 443–454
49. Ohring M (1992) *The materials Science of thin films*. Academic Press Limited, London, pp 419–420
50. www.matweb.com (accessed 9 January 2016)
51. www.azom.com (accessed 9 January 2016)
52. Pershin V, Lufitha M, Chandra S, Mostaghimi J (2003) Effect of substrate temperature on adhesion strength of plasma-sprayed nickel coatings. *J Therm Spray Technol* 12:370–376
53. Ahmed R, Faisal NH, Paradowska AM, Fitzpatrick ME (2012) A comparison of neutron diffraction and hole-drilling residual strain measurements in thermally sprayed coatings. *Surf Coat Technol* 206:4180–4185

54. Ahmed R, Yu H, Stewart S, Edwards L, Santisteban J (2007) Residual strain measurement in thermal spray cermet coatings via neutron diffraction. *ASME J Tribol* 129:411–418
55. Zhang XC, Xu BS, Xuan FZ, Tu ST, Wang HD, Wu YX (2009) Porosity and effective mechanical properties of plasma-sprayed Ni-based alloy coatings. *Appl Surf Sci* 255: 4362–4371
56. Heimann RB, Graßmann O, Zumbrink T, Jennissen HP (2001) Biomimetic processes during *in vitro* leaching of plasma sprayed hydroxyapatite coatings for endoprosthetic applications. *Mat Wiss U Werkstofftech* 32:913–921
57. Lin B, Zabeen S, Tong J, Preuss M, Withers PJ (2015) Residual stresses due to foreign object damage in laser-shock peened aerofoils: simulation and measurement. *Mech Mater* 82:78–90